JOURNAL OF CATALYSIS 98, 150–165 (1986)

Reduction of Nitric Oxide with Carbon Monoxide on the Rh(100) Single-Crystal Surface

RONALD E. HENDERSHOT[1] AND ROBERT S. HANSEN

Ames Laboratory, USDOE, and Department of Chemistry, Iowa State University, Ames, Iowa 50011

Received May 8, 1985; revised September 17, 1985

The reduction of nitric oxide with carbon monoxide has been investigated on the Rh(100) single-crystal surface. Steady-state kinetic measurements, at 688 K and in the pressure range 1.0 to 1800 Pa, indicate that this process proceeds via a Langmuir–Hinshelwood-type mechanism and is selective toward the production of N_2 and CO_2. The carbon monoxide kinetic order varied continuously from +1 to −1 as the partial pressure of CO was increased from 1 to 250 Pa, at a constant NO partial pressure of 57.5 Pa. In a similar manner, the nitric oxide kinetic order varied continuously from $+\frac{3}{2}$ to −1 as the partial pressure of NO was increased from 1 to 1800 Pa, at a constant CO partial pressure of 44.0 Pa. The catalyst surface was characterized with Auger electron spectroscopy (AES), low-energy electron diffraction (LEED), and thermal desorption spectroscopy (TDS). Initial Auger analysis revealed surface contamination by sulfur, phosphorus, and boron. The boron contaminant was identified by AES and by the formation of boron (3 × 1) or (3 × 3) ordered overlayers. These contaminants were removed via cycles of argon ion bombardment, reactive ion bombardment, and high-temperature annealing. Nitric oxide adsorbed with a high sticking coefficient and formed a $c(2 \times 2)$ ordered overlayer at saturation. The nitric oxide adsorbate dissociated upon slow stepwise heating as indicated by the production of a surface oxide and disappearance of surface nitrogen. Thermal desorption experiments at a faster heating rate indicated, however, that most of the adsorbed nitric oxide desorbed molecularly in a first-order process with a peak at 401 K during the temperature flash. Carbon monoxide adsorbs molecularly in two distinct sites with desorption from both following first-order kinetics with TDS peaks at 373 and 425 K. A kinetic model was developed which is consistent with both the steady-state kinetic and surface characterization results. The kinetic data were fit to the steady-state rate law derived from this mechanism involving the reduction of adsorbed nitrous oxide and nitrogen dioxide species by molecularly adsorbed carbon monoxide.

INTRODUCTION

The reduction of nitric oxide has been studied extensively in recent years and has been the subject of several reviews (*1–3*). This work is motivated at least in part by the effort to remove nitric oxide from various exhaust streams to improve air quality. The most effective catalyst from a practical standpoint is supported rhodium metal, due primarily to its ability to reduce NO selectively to N_2 under automotive exhaust conditions (*4–6*).

The mechanism of nitric oxide reduction is unclear and there have been relatively few mechanistic studies examining the NO/CO process on well-characterized rhodium surfaces. Campbell and White (*7*) utilized flash desorption spectroscopy (FDS), titration, and steady-state kinetics to examine nitric oxide reduction with carbon monoxide on polycrystalline rhodium wire. These authors reported that adsorbed nitric oxide dissociates into adsorbed atomic nitrogen and oxygen. Two adsorbed nitrogen atoms combine and desorb as molecular nitrogen. The adsorbed oxygen reacts with either adsorbed or gas-phase carbon monoxide to form the carbon dioxide product. These results were based primarily on the FDS and titration experiments and a detailed kinetic analysis was not performed. Dubois *et al.* (*8*) have recently reported evidence for

[1] Present address: MASTL, Dow Chemical U.S.A., 1604 Bldg., Midland, Mich. 48667.

0021-9517/86 $3.00

an oxygen intermediate in the NO/CO process on the Rh(331) single-crystal surface utilizing high-resolution electron energy loss spectroscopy (HREELS). These authors conclusively illustrated the existence of a surface oxide after a 1-L (1 L (Langmuir) = 1.333×10^{-4} Pa sec) nitric oxide exposure and subsequent flash to 450 K. In addition, both Auger electron spectroscopy (AES) and HREELS demonstrated the lack of surface nitrogen after this procedure, indicating that the formation of gas-phase molecular nitrogen is a fast process under these reaction conditions. A detailed steady-state kinetic study for the reduction of nitric oxide on well-characterized rhodium surfaces has not been reported previously.

The reduction of nitric oxide on supported rhodium catalysts has been reported extensively (*4–6, 9–13*). The formation of an isocyanate intermediate has been reported by several of these authors as an important intermediate in the formation of ammonia during the NO/CO process in the presence of water. The role of the isocyanate intermediate in the selective reduction of NO to N_2 is unclear. For supported rhodium catalysts, the reduction of NO with CO will yield, in general, both nitrous oxide and molecular nitrogen as products. For example, Rives-Arnau and Munuera (*9*) reported that the amount of nitrous oxide produced during the reduction of NO with CO reached a maximum at roughly 500 K, and subsequently decreased with increasing temperature for Rh/SiO_2. In addition, Arai and Tominaga (*10*) reported infrared spectroscopic evidence for the isocyanate intermediate and proposed a mechanism for the formation of the nitrous oxide and molecular nitrogen products via a Rh(NO)(CO) intermediate.

The results reported here consist of a detailed examination of the steady-state kinetics of the selective reduction of NO with CO to molecular nitrogen and carbon dioxide on the Rh(100) surface. The initial reaction rate was determined over a wide variety of process conditions in the pressure range between 1 and 1800 Pa. The catalyst surface was characterized with Auger electron spectroscopy (AES), low-energy electron diffraction, (LEED), and thermal desorption spectroscopy (TDS). These results were used to develop a chemically reasonable mechanism consistent with both surface characterization and steady-state kinetic results.

EXPERIMENTAL

The apparatus and procedures used during this investigation have been described in detail previously (*14, 15*). Only a brief summary will be given here. The schematic of the ultrahigh vacuum system used for the steady-state kinetic and thermal desorption experiments is shown in Fig. 1. A capacitance manometer was used to accurately measure the partial pressure of the reactant gases. A variable leak valve was used to continuously sample the gas phase in the reaction cell. The composition of this sample was determined with a quadrupole mass spectrometer (UTI 100-C).

Sample preparation. The Rh(100) single-crystal sample was cut using spark erosion from a macroscopic single-crystal rod obtained from Materials Research Corporation. The sample was aligned via the stan-

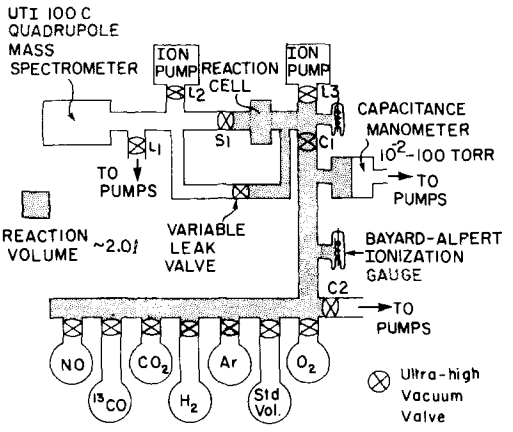

FIG. 1. Schematic drawing of ultrahigh vacuum system used for steady-state kinetic and thermal desorption experiments.

dard Laue X-ray backscattering methods. The cut single-crystal disk was mechanically polished to a mirror finish, and was within 1 degree of the desired orientation. The catalyst sample was essentially cylindrical in shape with a diameter of 0.7 cm, and was 0.75 mm thick. The total surface area of this sample was 0.93 cm^2, of which 82% consisted of the Rh(100) single-crystal surface, the remaining 18% being edge area. This disk was then mounted in the reaction cell by spotwelding a 0.25-mm tungsten support wire directly on the sample, which was then spotwelded to a 1.1-mm tungsten support rod mounted in the reaction cell. The temperature of the sample was monitored with a 0.076 mm tungsten/5% rhenium, tungsten/26% rhenium continuous thermocouple, which was spotwelded directly onto the rhodium surface.

The sample was cleaned, prior to the kinetic rate measurements, via numerous cycles of oxidation, reduction, and high-temperature annealing. Several procedures for the preparation of atomically clean rhodium surfaces have been reported in the literature (*7, 8, 16–19*) and similar procedures were used in this study. In the kinetic system, shown in Fig. 1, the criterion for a clean sample was necessarily that which produced a relatively high and reproducible reaction rate. Initially the catalytic activity of the Rh(100) sample was low and erratic. This was attributed to surface segregation of boron from the bulk of the sample. After numerous cycles of oxidation, reduction, and high-temperature annealing the reaction rate increased significantly and was reproducible to within 15%.

Surface characterization procedure. The catalyst was characterized with AES, LEED, and TDS. The AES and LEED analysis were performed in a Varian ultrahigh vacuum surface analysis system equipped with four-grid LEED optics, for LEED analysis, and a single-pass cylindrical mirror analyzer (CMA), for Auger electron detection. Auger electron spectra were recorded in the derivative mode using a phase-sensitive detection method employing a lock-in amplifier at a frequency of 17 kHz with a modulation voltage of 5 V peak to peak. A coaxial electron gun, operating at a beam energy of 2 keV and a beam current of 0.5 μA, was used to produce the core holes. The Rh(100) sample was mounted on a rotatable offset precision x,y,z manipulator with a continuous thermocouple (W/5% Re, W/26% Re) mounted mechanically between the crystal sample and an indirect resistive heater. This arrangement allowed the sample to be heated in the range 300 to 1500 K. In addition, an ion gun was available for the purpose of cleaning the sample. The LEED patterns were obtained using the four-grid LEED optics at energies between 50 and 250 eV, and were recorded using high speed Polaroid film. The surface analysis chamber was connected to an UHV gas manifold, via a variable leak valve, which allowed the sample to be exposed to the gas of interest.

Thermal desorption analysis was performed in the steady-state kinetic system shown in Fig. 1. The Rh(100) was cleaned prior to the TDS experiments as described in the preceding section. Thermal desorption spectra were obtained for NO, CO, and CO_2 at doses ranging from 0.01 to 100 L. The sample temperature was ramped from 300 to 1048 K radiantly at 10 K/sec while differentially pumping the cell. The desorption peaks were observed by monitoring mass spectrometer ion currents as functions of temperature. Due to the strong interaction of nitric oxide with glass walls of the reaction cell, these were heated to 150°C during the thermal desorption experiments involving nitric oxide.

Kinetic procedure. The reduction of nitric oxide with carbon monoxide on the Rh(100) single-crystal surface was studied at a temperature of 688 K and in the pressure range of 1.3 to 6700 Pa. During a reaction run the catalyst temperature was maintained, to ±3K, utilizing the focused light from a 1200-W projector bulb. This heating

method limited the temperature to a maximum of approximately 600°C, due to thermal conductivities of the reactant gases. The reduction of nitric oxide with carbon monoxide on rhodium metal produces three possible products, namely, N_2, N_2O, and CO_2, as shown in

$$NO + CO \rightarrow \tfrac{1}{2}N_2 + CO_2 \quad (1)$$

$$2NO + CO \rightarrow N_2O + CO_2. \quad (2)$$

In order to distinguish between the possible formation of the nitrous oxide and carbon dioxide products, labeled carbon-13 monoxide was used as a reductant during this mechanistic investigation. Under all reaction conditions examined during this study, carbon dioxide and nitrogen were the only products observed in the gas phase. In general, the progress of the reaction as a function of time was continuously monitored by the change in the peak height of the $^{13}CO_2$ (m/z = 45) mass peak. Since only initial rates were measured, this peak height had a linear time dependence. The reaction rate was calculated using the linear least-mean-squares regression line of the time dependence of the $^{13}CO_2$ product peak.

The reaction rate was determined over a wide range of initial conditions. The procedure used to determine the reaction rate under a given set of conditions involved the following steps. First, the catalyst was cleaned prior to each kinetic run by reduction in hydrogen (12.0 Pa, 400°C, 15 min), followed by high-temperature annealing (650°C, 10 min). The catalyst was then preheated to the desired reaction temperature, usually 688 K, with valve C1 closed. The appropriate partial pressure of each reactant was admitted into the gas manifold from the respective gas storage bulb, using the capacitance manometer to measure the partial pressure. With valves S1 and L3 closed, and the variable leak valve previously opened to a calibrated position, the catalytic reaction was initiated by simply opening valve C1. The extent of the reaction was continuously monitored by the differentially pumped quadrupole mass spectrometer, which analyzed a small sample of the gas phase via the variable leak valve. This valve allowed only a small portion, generally less than 1% of the reactor gas phase, to be removed from the catalytic reaction cell during a reaction run, which therefore operated as a static batch reactor. This procedure facilitated the measurement of the reaction product distribution, as well as the initial reaction rate, over a wide range of initial conditions. The reaction rate was converted to a turnover number (molecules/cm^2-sec) using several known system parameters. These included the reaction volume (1.99 liters), catalyst surface area, and mass spectrometer sensitivity, which was empirically determined and periodically checked. The reaction rate determined in this manner was reproducible to within 15%.

Materials. The oxygen (99.995%), nitrogen (99.998%), argon (99.9995%), hydrogen (99.998%), and carbon dioxide (99.998%) were obtained in 1-liter glass bulbs with break seals from the Linde Division of the Union Carbide Corporation and were used without further purification. The nitric oxide (98.5%) was obtained in a lecture bottle, also from the Linde Division. Mass spectrometer analysis showed the major impurities to be other oxides of nitrogen, carbon monoxide, nitrogen, and a trace amount of argon. This gas was then vacuum distilled and loaded into 1-liter Pyrex bulbs with break seals. Subsequent mass analysis showed no significant impurities. The carbon-13 monoxide was obtained from the Mound Laboratory Division of the Monsanto Corporation and had a 99% enrichment of carbon-13. The ^{13}CO (98%) contained 2% of argon and no other detectable impurities; this gas was used without further purification.

RESULTS AND DISCUSSION

Surface Characterization

The catalyst surface was characterized

with a series of LEED/Auger and thermal desorption experiments. The objectives of these experiments were to establish a cleaning procedure and to characterize the adsorption–desorption properties of the reactants and products relevant to the mechanisms of NO reduction with CO. Several systematic studies of the adsorption–desorption properties of individual small molecules (i.e., NO, CO, H_2, O_2, N_2, etc.) on well-characterized rhodium surfaces have been reported previously (*7, 8, 16–18, 20*). The surface characterization portion of the present investigation served in part to confirm, in part to extend, these prior results.

A cut and polished Rh(100) single-crystal surface was mounted on an offset manipulator and placed in the LEED/Auger system. An initial Auger spectrum, as shown in Fig. 2, revealed surface contamination by phosphorus, sulfur, and boron. This result is fairly typical and numerous cleaning procedures have been reported to obtain a clean rhodium surface (*8, 14, 16, 18, 21*). The exact procedure used in this investigation involved high-temperature bombardment by reactive ion beams. The sulfur contaminant was removed by cycles of high-temperature hydrogen ion bombardment (1000 eV, 500°C, 20 min), followed by annealing of the sample (1000°C, 10 min). A similar procedure has been reported previously for removing carbon, sulfur, and oxygen from copper and steel surfaces (*22*). Phosphorus was similarly removed by cycles of high-temperature oxygen ion bombardment (1000 eV, 500°C, 10 min) followed by annealing of the sample (1000°C, 10 min). This procedure yielded a relatively clean surface, contaminated only with boron, as shown in Fig. 2b.

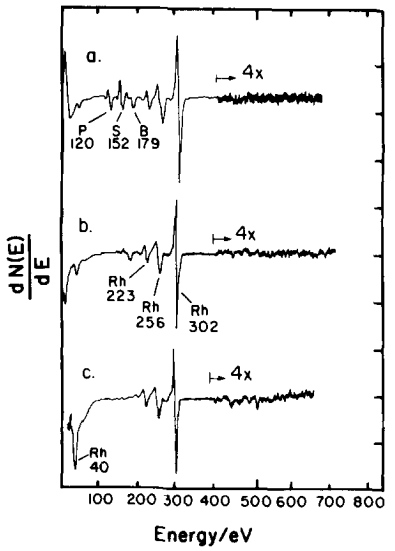

FIG. 2. Auger spectra of Rh(100) surface during cleaning procedure: (a) initial Auger spectrum; (b) Auger spectrum after H_2 and O_2 bombardment; (c) Auger spectrum of clean Rh(100).

The boron surface contaminant was extremely resistant to the above cleaning procedure and could be removed only via numerous cycles of argon ion bombardment (3 keV, 25°C, 60 min), followed by high-temperature annealing (1000°C, 10 min). During this procedure it was noted that boron segregated to the surface from the bulk at temperatures greater than about 750°C. Initially upon surface segregation the boron formed a (3 × 1) ordered overlayer, and as boron was depleted from the bulk it then segregated to a lesser extent and formed a (3 × 3) ordered overlayer. A similar (3 × 1) overlayer has been observed previously (*23*) but not identified as boron. Once segregated to the surface, this boron could be reversibly oxidized (1.3×10^{-3} Pa O_2, 500°C, 1 min), and then reduced by high-temperature annealing (1000°C, 5 min). The boron oxide formed, most probably BO_2^- (*21, 23*), could be identified by its characteristic Auger peak at 171 eV. Eventually a clean surface could be prepared using a single cycle of argon ion bombardment (3 keV, 25°C, 60 min), followed by a high-temperature flash to repair the lattice damage (500°C, 30 sec). The surface prepared in this manner exhibited no detectable impurities by AES, as shown in Fig. 2c, and displayed a sharp (1 × 1) LEED pattern.

Auger analysis of the adsorption of carbon monoxide gave results similar to those reported previously by Castner *et al.* (*16*) and thus will not be discussed here. It is

noteworthy to mention that no conclusive evidence for carbon monoxide dissociation was observed during this investigation. Dissociation of carbon monoxide induced by the probing electron beam was observed and this effect has been reported previously (*24*).

Nitric oxide adsorbs with a high sticking coefficient and at saturation forms a $c(2 \times 2)$ overlayer, which has been reported previously (*16*). In order to characterize the thermal stability of this overlayer, the sample was heated to successively higher temperatures for 10 min; Auger spectra were subsequently recorded at room temperature. The results are shown in Fig. 3. The nitric oxide adsorbate is relatively stable up to 200°C, showing only a small drop in coverage, as indicated by the small drop in Auger peak intensity. This small drop is most likely due to molecular nitric oxide desorption occurring at approximately 400 K. At about 575 K, a precipitous drop in the nitrogen peak intensity occurs, while the oxygen Auger peak remains relatively unaffected. At about 875 K, the oxygen Auger peak decreases likewise, and is essentially zero at 975 K. These results indicate competition between two processes, namely, molecular NO adsorption–desorption and NO dissociation followed by N_2 desorption. The oxygen adsorbate either desorbs as O_2 or diffuses into the bulk, a process previously reported to occur (*16, 25*). These results are in general agreement with the NO adsorption results reported previously (*7, 8, 16–18, 20*).

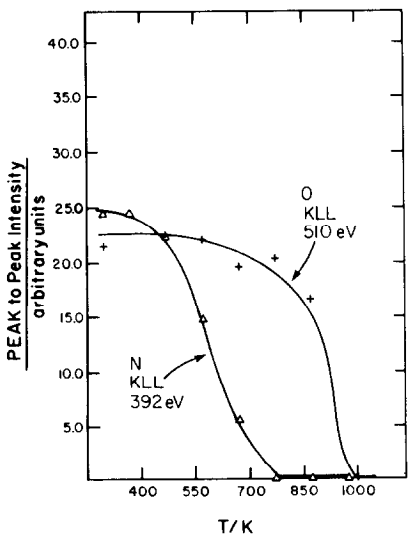

FIG. 3. Thermal stability of adsorbed nitric oxide as determined using the N and O KLL Auger peaks.

The interaction of nitrogen and carbon dioxide likewise follows results published previously (*7, 8, 16–18, 20*). The adsorption of carbon dioxide produced a $c(2 \times 2)$ ordered overlayer, as previously reported by Castner *et al.* (*16*) and considered to most probably represent dissociative adsorption into adsorbed carbon monoxide and oxygen. All attempts to adsorb molecular nitrogen failed.

In an effort to examine the state of the catalyst under reaction conditions, a coadsorption experiment was performed with a 1/1 mixture of NO/CO at 688 K, and a total pressure of 8×10^{-3} Pa. The result of this experiment is summarized in

$$(1 \times 1)\ \mathrm{Rh} \xrightarrow[688\ \mathrm{K},\ 5\ \mathrm{min}]{8 \times 10^{-3}\ \mathrm{Pa},\ \mathrm{NO/CO}} \begin{matrix} c(2 \times 2) \\ \mathrm{O(ads)}\ 0.08 - 0.05 \\ \mathrm{N(ads)}\ 0.09 - 0.20. \\ \mathrm{C(ads)}\ 0.21 - 0.13 \end{matrix} \quad (3)$$

The range of coverage reported here represents the two methods used to record the Auger spectra. The figures in the left-hand column represent the calculated coverages, if the gas phase is removed first and then the substrate is reduced to room temperature, prior to recording the Auger spectra. The figures in the right-hand column represent the reverse of that process prior to the Auger experiment. These coverages were calculated utilizing published sensitivities (*26*), and are based upon the peak intensity of the C, O, and N KLL Auger lines, relative to the Rh MNN Auger line at 302 eV. The absolute calibration was based on the oxygen KLL Auger peak of the 0.25 monolayer $p(2 \times 2)$ oxygen ordered overlayer. Several points should be made at this time concerning the results of this experiment. First, the surface contains a significant

amount of adsorbed nitrogen, and second the surface is not extensively oxidized under these reactions conditions. It has been concluded by previous workers (*7, 8*) that the surface coverage of nitrogen was negligible during the reduction of nitric oxide with carbon monoxide. These conclusions were based upon nitric oxide adsorption at room temperature, and a total pressure in the 1.3×10^{-5} Pa range, followed by heating the sample *in vacuo*. The present Auger experiment involves NO/CO coadsorption at 688 K, in the 1.3×10^{-3} Pa range.

The catalyst surface was further characterized with a series of thermal desorption experiments. A series of carbon monoxide thermal desorption spectra, as a function of ^{13}CO exposure, are shown in Fig. 4. The corresponding dependence of desorption peak area as a function of exposure is shown in Fig. 5. At exposures less than 1.0 L, carbon monoxide desorbs in a first-order process with a peak maximum at 425 K. At higher exposures, on the order of 5.0 L, a low-temperature desorption peak is observed at about 373 K. The Rh(100) surface

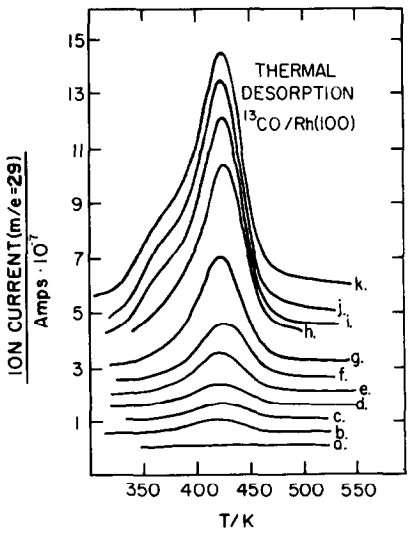

FIG. 4. ^{13}CO thermal desorption spectra recorded with a heating rate $\beta = 10.7$ K/sec after various ^{13}CO exposures at 300 K: (a) background; (b) 0.01 L; (c) 0.02 L; (d) 0.05 L; (e) 0.10 L; (f) 0.22 L; (g) 0.50 L; (h) 1.02 L; (i) 2.02 L; (j) 5.20 L; (k) 10.1 L. Curves have been shifted toward upward slightly for greater clarity.

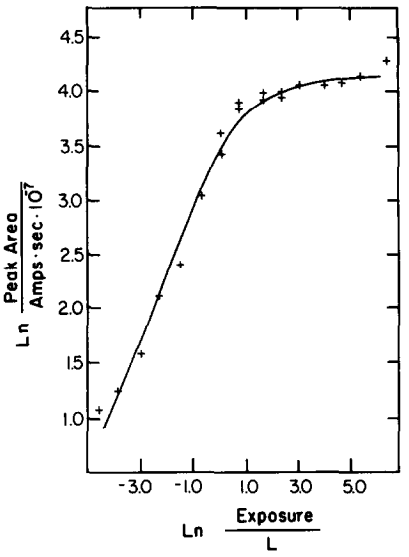

FIG. 5. ^{13}CO desorption peak area–exposure relationship illustrating saturation exposure at about 2.0 L.

reaches saturation coverage of CO at about 2.0 L, as shown in Fig. 5. The high-temperature peak represents molecular adsorption at an atop site, while the low temperature shoulder indicates population of the surface by a bridge-bonded species. The heat of desorption for these two sites was calculated according to the procedure developed by Redhead (*27*). The difference of the heat of desorption between these two sites was calculated to be 3.2 kcal/mole, which is similar to a previous result (*16*). The calculated heat of desorption for the atop site is 25.5 kcal/mole, which is somewhat lower than that reported by previous workers (*16, 17, 28*). The reason for this discrepancy is not known.

A series of thermal desorption experiments was performed to elucidate the adsorption–desorption characteristics of nitric oxide. The desorption peaks observed after a 0.11-L NO exposure of the catalyst surface are shown in Fig. 6. Desorption of nitric oxide is somewhat more complex than that of carbon monoxide; however, several features are readily apparent after a close examination of Fig. 6. A large amount of the adsorbed nitric oxide desorbs in a

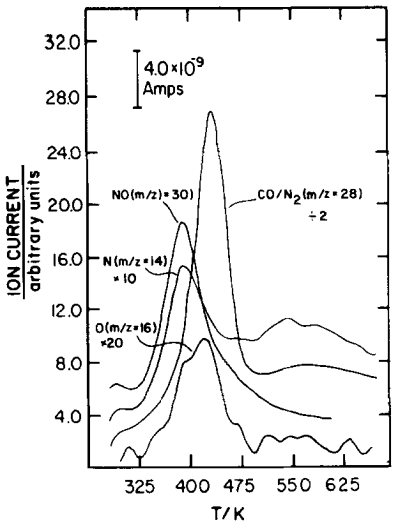

FIG. 6. NO (m/z = 30), CO/N_2 (m/z = 28), N (m/z = 14), and O (m/z = 16) desorption spectra recorded after a 0.11-L NO exposure at 315 K and with a heating rate of β = 11.5 K/sec.

molecular NO peak at 392 K. Two peaks with m/z = 28 are observed, a large desorption peak at 436 K and a broad peak between 523 and 660 K. It is clear, after an examination of the atomic nitrogen peak at m/z = 14 and the atomic oxygen peak at m/z = 16, that the m/z = 28 peak at 436 K represents CO desorption from the sample. This peak corresponds to the molecular desorption of CO, as shown in Fig. 4, and corresponds to an exposure of less than 0.008 L of CO, as calibrated in Fig. 5. The broad m/z = 28 peak between 523 and 625 K clearly represents molecular nitrogen desorption, since both the m/z = 14 and m/z = 28 signals exhibit maxima in this region. Molecular nitrogen desorption peaks have been reported previously at 523 K for the Rh(110) surface (*17*), and a broad peak between 480 and 650 K for polycrystalline rhodium wire (*7*). The amount of molecular NO desorbing from the polycrystalline wire surface was quite small, whereas the amount of molecular nitrogen desorbing from this wire surface was quite large (*7*). The situation with NO desorption from the Rh(100) surface, as shown in Fig. 6, is the reverse of that reported for the polycrystalline wire surface.

A series of NO desorption spectra at various exposures is shown in Fig. 7, with the corresponding peak area dependence shown in Fig. 8. Nitric oxide desorbs in a first-order desorption peak with a peak maximum at 401 K, and reaches saturation at about 2.0 L. The corresponding heat of desorption, using as before the method developed by Redhead (*27*), is 24.0 kcal/mole which compares favorably with the heat of desorption of NO from polycrystalline Rh wire of 25 kcal/mole (*7*). These results complement those reported earlier for nitric oxide adsorption on polycrystalline rhodium wire (*7*); stepped rhodium single-crystal surfaces, namely, the Rh(331) (*8*, *18*) and Rh(755) (*18*); and the corrugated Rh(110) (*17*) surface. In addition, these results are in basic agreement with a recently published report on NO desorption from the Rh(100) surface (*29*). The general results of the above authors, for NO adsorption on these rhodium surfaces, are dissociative adsorption at low exposures (i.e., <1.0 L) and molecular adsorption at higher exposures

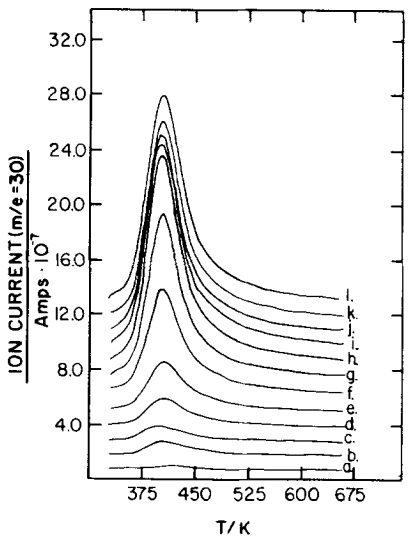

FIG. 7. NO thermal desorption spectra recorded with a heating rate β = 11.6 K/sec after various NO exposures at 315 K: (a) background; (b) 0.01 L; (c) 0.02 L; (d) 0.104 L; (e) 0.21 L; (f) 0.51 L; (g) 0.99 L; (h) 1.99 L; (i) 5.00 L; (j) 10.1 L; (k) 19.9 L; (l) 49.8 L. Curves have been shifted upward slightly for greater clarity.

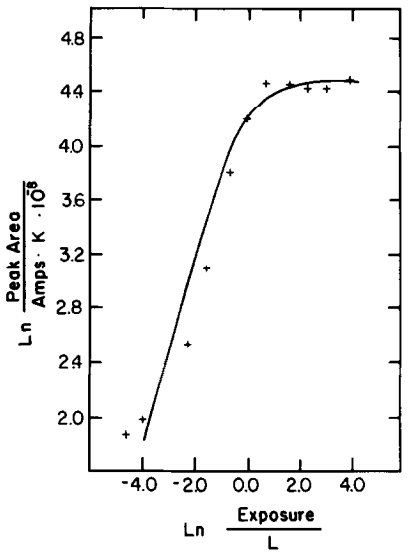

FIG. 8. NO desorption and peak area–exposure relationship illustrating saturation exposure of 2.0 L.

(i.e., >1.0 L). It is difficult to quantitatively separate molecular from dissociative adsorption since dissociation undoubtedly occurs during the flash heating. These results do indicate, however, that molecular NO desorption and surface NO dissociation are competing processes. Periodic trends described by Benziger (*30*), Broden *et al.* (*31*), and Miyazaki and Yasumori (*32*) place rhodium on the dividing line between molecular and dissociative NO adsorption. It is expected, therefore, that surface geometry would have an effect on the ability of rhodium surfaces to dissociate nitric oxide. Thus one would expect that the more energetic surfaces (i.e., stepped, kinked, corrugated, and polycrystalline) would exhibit a greater tendency to dissociate NO than the smooth Rh(100) surface. This is indeed the case.

A comparison of Figs. 3 and 6 clearly illustrates the competition between nitric oxide molecular adsorption–desorption and surface dissociation. As illustrated in Fig. 3 a small molecular desorption peak occurs at about 400 K, but a large extent of dissociation is indicated by the separate decline of the nitrogen and oxygen KLL Auger lines. In Fig. 6, however, most of the adsorbed nitric oxide seems to desorb in a molecular form. Evidently the slow stepwise heating procedure used for the experiment described in Fig. 3 favors the dissociation process, but the rapid temperature rise used during the thermal desorption procedure favors molecular desorption.

Several conclusions can be made at this point with respect to the reduction of NO with CO on the Rh(100) single-crystal surface. First, the carbon monoxide reactant is expected to interact with this surface in a purely molecular fashion, serving simply to reduce some surface oxygen species, produced by the interaction of nitric oxide with the catalyst surface. This molecular CO interaction would be consistent with the TDS and Auger results. The interaction of NO with the catalyst surface under reaction conditions is not clear, at this point. It is apparent that both molecular and dissociated nitric oxide should play a role in the NO/CO process. The relative amounts of these forms should depend upon the gas-phase composition and the interactions between adsorbed species on the catalyst surface under reaction conditions. In addition the products formed, namely, N_2 and CO_2 are expected to have little effect upon the reaction rate as measured in this study. Molecular nitrogen, simply because it will not adsorb under reaction conditions of the kinetic experiments, should have little effect on the rate of reaction. Thermal desorption results indicate that the sticking coefficient of carbon dioxide is five times smaller than that of carbon monoxide, in agreement with results of Castner *et al.* (*16*). This fact coupled with the low carbon dioxide partial pressure present under the reaction conditions of this study, as compared to the carbon monoxide concentration, indicates that the CO_2 produced during the kinetic measurements will not inhibit the initial reaction rate.

Kinetic Results

The steady-state kinetics of NO reduc-

tion with CO was studied over a wide range of initial conditions. This wide variation is important in heterogeneous kinetics, because reactant orders are necessarily functions of partial pressures. The reaction rate as a function of carbon monoxide partial pressure, at a constant nitric oxide partial pressure of 57.5 Pa and a constant reaction temperature of 688 K, is shown in Fig. 9. As expected, the carbon monoxide order is a function of carbon monoxide partial pressure. In particular, the carbon monoxide order is approximately first order in the partial pressure range from 1.3 to 5.0 Pa. Between 5.0 and 54.0 Pa, the order with respect to carbon monoxide gradually decreases to zero, and finally between 54.0 and 250 Pa the carbon monoxide order is inverse first order. This dependence on carbon monoxide partial pressure is typical of Langmuir–Hinshelwood heterogeneous kinetics.

The reaction rate as a function of nitric oxide partial pressure, at constant carbon monoxide partial pressure of 44.0 Pa and constant reaction temperature of 688 K, is shown in Fig. 10. The nitric oxide order

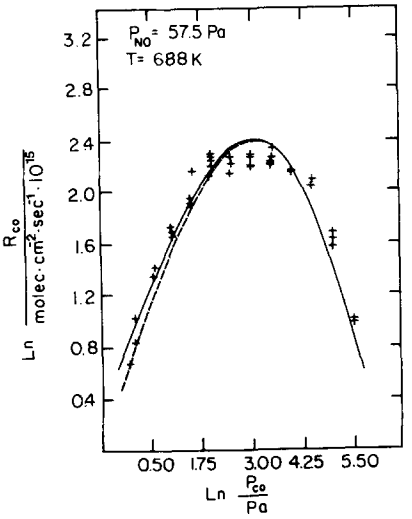

FIG. 9. Carbon monoxide order plot determined using a constant nitric oxide pressure of 57.5 Pa at 688 K. Solid and dashed curves correspond to models culminating in Eqs. (30) and (25), respectively, with parameters given in Table 1.

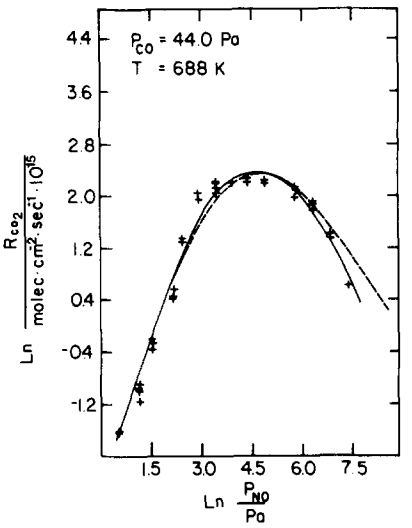

FIG. 10. Nitric oxide order plot determined using a constant carbon monoxide pressure of 44.0 Pa at 688 K. Solid and dashed curves correspond to models culminating in Eqs. (30) and (25), respectively, with parameters given in Table 1.

plot illustrates a behavior very similar to that of the carbon monoxide order plot. In particular, the order with respect to nitric oxide is 1.5, in the partial pressure range between 1.5 and 20 Pa NO, gradually decreasing to zero order, and finally decreasing to approximately inverse first order between 400 and 1800 Pa NO. The nitric oxide order plot together with the carbon monoxide order plot implies that the reduction of nitric oxide with carbon monoxide follows Langmuir–Hinshelwood kinetics.

The dependence of the reaction rate on the partial pressure of each of the reaction products was determined; these data are shown in Fig. 11. The reaction order with respect to the partial pressure of nitrogen is zero, over the partial pressure range between 1 and 200 Pa, as expected since molecular nitrogen will not chemisorb on the catalyst surface under reaction conditions. In a similar fashion, the order with respect to carbon dioxide is also zero, over the partial pressure range 1–200 Pa. This is also the expected result, since carbon dioxide would not be able to compete effectively for surface sites in the presence of carbon mon-

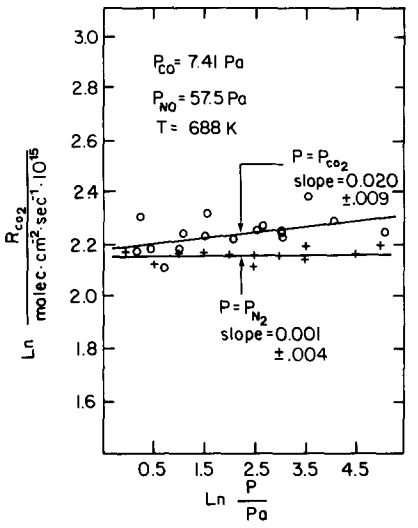

FIG. 11. Nitrogen and carbon dioxide order plots determined using a constant carbon monoxide pressure of 7.41 Pa and a constant nitric oxide pressure of 57.5 Pa at 688 K. Slopes calculated by linear least-square fits of the rate data are given; within experimental error, they can be taken as zero.

oxide and nitric oxide. These two order plots imply that under reaction conditions, the elementary reaction steps directly involved in the formation of reaction products are essentially irreversible.

The temperature dependence of the reaction rate is shown in Fig. 12, in the form of a standard Arrhenius plot. The temperature behavior of the reaction rate does not produce a straight line on the Arrhenius plot, and this is not unusual for a heterogeneous catalytic reaction. The slope of the tangent to this curve, at any given temperature, is proportional to the apparent activation energy of this process. In particular, the apparent activation energy at 688 K (i.e., the temperature used for the collection of the reactant/product order plots) is approximately 3.2 kcal/mole. As temperature decreases, the apparent activation energy increases at constant gas-phase composition. This effect is primarily due to the inability of nitric oxide to displace carbon monoxide at these lower temperatures. A similar effect has been reported for the NO/CO reaction on polycrystalline rhodium wire (*7*).

Mechanistic Considerations

As a starting place for examining the proposed mechanism of the NO/CO process, it is useful to consider a recently proposed mechanism (*8*):

$$CO(g) + * \leftrightarrow CO(ads) \quad (4)$$

$$NO(g) + * \leftrightarrow NO(ads) \quad (5)$$

$$NO(ads) + * \rightarrow N(ads) + O(ads) \quad (6)$$

$$2N(ads) \rightarrow N_2(g) + 2* \quad (7)$$

$$CO(ads) + O(ads) \rightarrow CO_2(g) + 2* \quad (8)$$

This mechanism has been supported by AES, TDS, and HREELS results on the Rh(331) single-crystal surface (*8*). The rate law for this mechanism is given by Eq. (9) where [*] denotes the concentration of vacant active sites, and [$\overset{*}{N}O$] denotes the fractional coverage of adsorbed nitric oxide.

$$\text{Rate} = \frac{dP(CO_2)}{dt} = k_6 [\overset{*}{N}O] [*] \quad (9)$$

$$1.0 = [*] + [\overset{*}{C}O] + [\overset{*}{N}O] + [\overset{*}{N}] + [\overset{*}{O}] \quad (10)$$

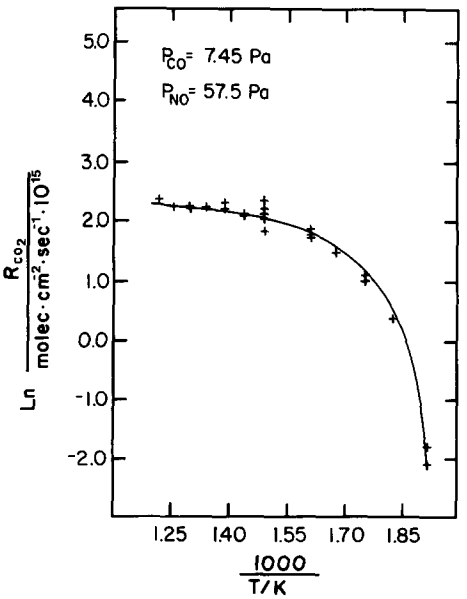

FIG. 12. Temperature dependence of reaction rate using a constant carbon monoxide pressure of 7.45 Pa and a constant nitric oxide pressure of 57.5 Pa.

Utilizing the site balance given in Eq. (10), and applying the usual steady-state assumptions, the reaction rate equation in terms of the reactant partial pressures can be derived, and this is given in

$$\text{rate} = \frac{d(CO_2)}{dt} = \frac{k_6 K_5 P_{NO}}{\left(1.0 + K_4 P_{CO} + K_5 P_{NO} + \frac{K_5 k_6}{2k_7} P_{NO}^{1/2} + \frac{K_5 k_6}{K_4 k_8} \frac{P_{NO}}{P_{CO}}\right)^2} \cdot \quad (11)$$

This mechanism is supported primarily by spectroscopic evidence at a total pressure in the 6.7×10^{-5} Pa range. There are currently no steady-state kinetic data which support this mechanism.

A close examination of Eq. (11) indicates that the order with respect to carbon monoxide depends upon the partial pressure of carbon monoxide, at constant partial pressure of NO. This equation predicts that the CO order should vary between 2.0 at low P(CO), and -2.0 at high P(CO). The nitric oxide order changes in a similar fashion between 1.0 at low P(NO) and -1.0 at high P(NO) at constant P(CO). A comparison between the limiting orders predicted by Eq. (11) and the limiting orders as observed in this kinetic study, shown in Figs. 9 and 10, clearly demonstrates inconsistency. In particular, the 3/2 order with respect to nitric oxide, at low P(NO) and constant P(CO), suggests that the mechanism of the NO/CO process is more complex than the mechanism given in Eqs. (4)–(8).

It is well known that for supported rhodium catalysts, at lower temperature, the products of the NO/CO process include carbon dioxide, nitrous oxide, and nitrogen (*9, 33, 34*). Thus it would be reasonable to include a nitrous oxide intermediate in the NO/CO process, as given in

$$CO(g) + * \leftrightarrow CO(ads) \quad (12)$$

$$NO(g) + * \leftrightarrow NO(ads) \quad (13)$$

$$2NO(ads) \leftrightarrow N_2O(ads) + O(ads) \quad (14)$$

$$N_2O(ads) + CO(ads) \rightarrow N_2(g) + CO_2(g) + 2* \quad (15)$$

$$O(ads) + NO(ads) \rightarrow NO_2(ads) + * \quad (16)$$

$$NO_2(ads) + CO(ads) \rightarrow CO_2(g) + NO(g) + 2*. \quad (17)$$

Assuming a steady-state formalism, together with the site balance given

$$1.0 = [*] + [\overset{*}{CO}] + [\overset{*}{NO}] + [\overset{*}{N_2O}] + [\overset{*}{NO_2}] + [\overset{*}{O}] \quad (18)$$

the rate equation can be easily derived as given in

$$\text{rate} = \frac{d(CO_2)}{dt} = \frac{F P_{NO}^{3/2} P_{CO}^{1/2}}{(1.0 + A P_{CO} + B P_{NO} + G P_{NO}^{3/2}/P_{CO}^{1/2} + E P_{CO}^{1/2} P_{NO}^{1/2})^2} \quad (19)$$

The parameters given in this equation, namely, A, B, G, E, and F, represent collections of rate and equilibrium constants, as given by Eqs.

$$A = K_{12} \quad (20)$$

$$B = K_{13} \quad (21)$$

$$G = \left(\frac{K_{13}^3 K_{14} k_{16}}{K_{12} k_{15}}\right)^{1/2} + \left(\frac{K_{13}^3 K_{14} k_{15} k_{16}}{K_{12} k_{17}^2}\right)^{1/2} \quad (22)$$

$$E = \left(\frac{K_{12} K_{13} K_{14} k_{15}}{k_{16}}\right)^{1/2} \quad (23)$$

$$F = (K_{12} K_{13}^3 K_{14} k_{15} k_{16})^{1/2}. \quad (24)$$

The limiting orders predicted by Eq. (19) with respect to nitric oxide for the low and high partial pressure extremes are $+\frac{3}{2}$ and $-\frac{3}{2}$ respectively. These limiting orders are consistent with the experimental order plot shown in Fig. 10, assuming, of course, that the high-pressure limit was not reached experimentally. Similarly, the limiting orders with respect to carbon monoxide, predicted

by Eq. (19), namely, $\frac{3}{2}$ to $-\frac{3}{2}$, are also consistent with the experimental order plot shown in Fig. 9, assuming once again that the extremes were not reached experimentally. The final test of the compatibility of the rate equation and the experimental reaction rate data would be a parametric fit of the data to the rate equation.

The complexity of Eq. (19) requires the fitting procedure to be accomplished via a nonlinear least-squares analysis. The algorithm used to fit the experimental data has been described in Haskell and Jones (*35*), and simply consists of a nonlinear least-squares analysis based upon grid minimization. During the fitting procedure it was determined that the values of the terms in the denominator containing the partial pressure variables were large compared to 1.0. This fact forces Eq. (19) to be rearranged, as shown in

$$\text{rate} = \frac{d(CO_2)}{dt} = \frac{P_{NO}^{3/2} P_{CO}^{1/2}}{\left(\frac{A}{F^{1/2}} P_{CO} + \frac{B}{F^{1/2}} P_{NO} + \frac{G}{F^{1/2}} \frac{P_{NO}^{3/2}}{P_{CO}^{1/2}} + \frac{E}{F^{1/2}} P_{CO}^{1/2} P_{NO}^{1/2}\right)^2}, \tag{25}$$

with the loss of a degree of freedom.

The best obtainable fit of Eq. (25), with chemically reasonable values (i.e., positive values) for the fitting parameters for the carbon monoxide and nitric oxide order plots, respectively, is shown as dashed curves in Figs. 9 and 10. The numerical values of the fitting parameters used for the calculated curves are given in the left-hand column of Table 1. As shown in these figures, the mechanism developed in Eqs. (12)–(17) quite adequately models the experimental data over the entire range of initial conditions, except in the limit of high nitric oxide partial pressure. In general, however, the model is quite satisfactory in the sense that it fits the experimental data.

The physical significances of the parameter values and of Eq. (25) can be partially but not completely developed from available information. The fact that the terms in the denominator are large compared to 1.0 indicates that the number of vacant active sites is quite small under reaction conditions. The remaining terms in the denominator are each proportional to the concentration of a reaction intermediate, as given in Eqs. (26)–(29).

$$\frac{[\overset{*}{CO}]}{[*]} = AP_{CO} \tag{26}$$

$$\frac{[\overset{*}{NO}]}{[*]} = BP_{NO} \tag{27}$$

$$\frac{[\overset{*}{N_2O}]}{[*]} + \frac{[\overset{*}{NO_2}]}{[*]} = G\frac{P_{NO}^{3/2}}{P_{CO}^{1/2}} \tag{28}$$

$$\frac{[\overset{*}{O}]}{[*]} = EP_{CO}^{1/2} P_{NO}^{1/2}. \tag{29}$$

From the values given in the left-hand column of Table 1, it is clear that the surface is covered primarily by adsorbed molecular carbon monoxide and nitric oxide. Due to the large number of steps in the reaction mechanism (i.e., six steps which yields six constants, three equilibrium constants, and three rate constants), it is impossible to solve explicitly for any of the thermodynamic or kinetic constants in the

TABLE 1

Values of the Constants Used to Fit the Experimental Order Plots to the Derived Steady-State Rate Laws

Constant	Values determined ($sec^{1/2}$ $molecule^{-1/2}$ cm)	
	For best fit to Eq. (25)	For best fit to Eq. (30)
$A/F^{1/2}$	5.78×10^{-9}	5.78×10^{-9}
$B/F^{1/2}$	4.62×10^{-9}	4.63×10^{-9}
$G/F^{1/2}$	4.26×10^{-10}	3.57×10^{-10}
$E/F^{1/2}$	0.0	0.0
$H/F^{1/2}$ (Pa^{-1})	—	1.08×10^{-12}

proposed mechanism, given only the values of the fitting parameters.

As mentioned previously, the mechanistic model described in Eqs. (12)–(17) does not adequately fit the dependence of the reaction rate at high nitric oxide partial pressures. From an empirical point of view the reaction rate decreases in this region faster than the theory predicts. Thus a higher order $P(NO)$ term would be necessary in the denominator of Eq. (25) for the theory to fully model the experimental data. Such an equation is given by

$$\text{rate } (CO_2) = \frac{P_{NO}^{3/2} P_{CO}^{1/2}}{\left(\frac{A}{F^{1/2}} P_{CO} + \frac{B}{F^{1/2}} P_{NO} + \frac{G}{F^{1/2}} \frac{P_{NO}^{3/2}}{P_{CO}^{1/2}} + \frac{E}{F^{1/2}} P_{CO}^{1/2} P_{NO}^{1/2} + \frac{H}{F^{1/2}} P_{NO}^2\right)^2}, \quad (30)$$

where the $(H/F^{1/2})P_{NO}^2$ term has been added in the denominator. Such a term would arise as the result of the addition of

$$NO(ads) \leftrightarrow (NO)_2(ads) + * \quad (31)$$

to the reaction mechanism given in Eqs. (12)–(17), with H as shown in Eq. (32).

$$H = K_{31} k_{13}^2 \quad (32)$$

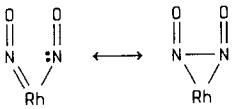

(33)

This intermediate might have the form described in Eq. (33). This surface structure has been supported previously by Ibach and Lehwald (*36*) using HREELS, although these results are subject to controversy (*37*). The best obtainable fit of the experimental data to Eq. (30) is shown as solid curves in Figs. 9 and 10, and the values of the fitting parameters are shown in Table 1. As shown in Fig. 9, the fits of the carbon monoxide order plot according to Eqs. (25) and (30) are essentially identical, however, the fit of Eq. (30) to the nitric oxide order plot indicates significant improvement in the high NO partial pressure region. This was expected since Eq. (30) was designed to have this effect. The existence of the intermediate given in Eq. (33) is debatable. Alternately, the breakdown of the kinetic model, given in Eqs. (12)–(17), at high nitric oxide partial pressures might be the result of adsorbate–adsorbate interactions.

This mechanism is also consistent with the surface characterization results. In particular, the thermal desorption analysis of carbon monoxide implies that under reaction conditions, a molecular adsorption–desorption equilibrium prevails. This is indeed the case in the proposed mechanism according to Eq. (12). In addition, Auger experiments described previously suggested that the catalyst surface was not extensively oxidized under reaction conditions. The concentration of adsorbed oxygen as a function of the reactant partial pressures is given in Eq. (29). Since the value for the parameter E determined during the fitting procedure was essentially zero, then the concentration of adsorbed oxygen as predicted by the kinetic model is also zero, in agreement with the Auger results. These results are in disagreement with earlier results which indicate that adsorbed oxygen plays an important role in the NO/CO process (*6, 10*). This is primarily due to the fact that the earlier studies were performed at a total pressure of approximately 6.7×10^{-5} Pa. The flux of reactant molecules to the surface at this pressure is low enough that the fraction of vacant active sites is relatively high. This permits the dissociation of nitric oxide to occur according to

$$NO(ads) + * \rightarrow N(ads) + O(ads). \quad (34)$$

Under the reaction conditions of this study, however, the reactant partial pressures are

relatively high (i.e., 13 Pa) and the fraction of vacant active sites is quite low. This would clearly inhibit the dissociation of nitric oxide. Thus it is not surprising that the kinetic data collected in this investigation cannot be described by the mechanism proposed earlier for the low-pressure studies.

This model implies the irreversibility of reaction steps given in Eqs. (15), (16), and (17). The irreversibility of Eqs. (15) and (17) is supported directly by the experimental product order plots, shown in Fig. 11. These order plots illustrate a zeroth order dependence of the reaction rate with respect to each product, and therefore steps (15) and (17) must be irreversible. The irreversibility of step (16) lacks any direct experimental evidence. However, if Eq. (16) is established as an equilibrium process, the resulting rate law does not model the experimental data in an acceptable manner.

Throughout this discussion, an asterisk has been used to denote a catalytic active site. While the exact nature of this site cannot be determined from the experimental evidence presented here, it is useful to examine possible structures of the reaction intermediates. Assuming an active site to be a single rhodium atom, then reasonable structures can be postulated for each of the reaction intermediates, as given in

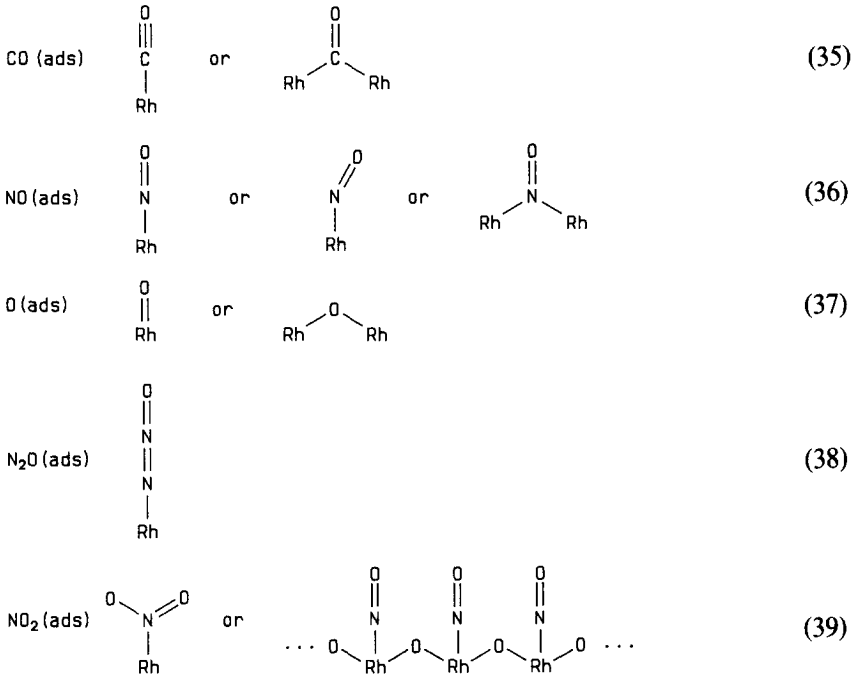

As shown in Eq. (35), carbon monoxide can adsorb in two possible sites, namely, the linear atop site and the bridge-bonded site. These two sites correlate well with the TDS results discussed in the previous section, and with LEED/Auger, HREELS, and IR results widely reported in the literature (*10, 16, 17, 20, 24, 28*). The adsorption of nitric oxide on the Rh(331) surface has been recently studied by Dubois *et al.* (*8*). These authors reported evidence using HREELS for both the bent and linear nitrosyls with the predominant species being the bent configuration; these are shown in Eq. (36). Several other geometries of nitric oxide bonding to transition metal surfaces have been reported previously, including a bridge-bonded species and the formation of surface NO^- and NO^+ species (*9, 10, 12, 36, 37*). In the work discussed above, Dubois *et*

al. (*8*) commented that HREELS results for the Rh(111) surface suggested the formation of at least five different adsorbed nitric oxide species. Oxygen adsorption on rhodium surfaces has been studied by numerous authors (*16, 18, 25, 28*), and the bonding geometries shown in Eq. (37) have been proposed. Reasonable structures for the nitrous oxide and nitrogen dioxide species are shown in Eqs. (38) and (39). It is noteworthy that the formation of adsorbed nitrous oxide and nitrogen dioxide species has been observed via IR after the interaction of carbon monoxide and nitric oxide on Rh/Al_2O_3 (*10*). Thus it seems quite reasonable to include these intermediates in the reduction of nitric oxide with carbon monoxide on the Rh(100) surface.

The mechanism presented in Eqs. (12)–(17) is consistent with both the steady-state kinetic and surface characterization results. This kinetic model is relatively simple; however, it is probably not unique. The fact that the derived rate law is consistent with the experimental data provides only a necessary, but not sufficient, condition that this model is the correct mechanism. The mechanism proposed in Eqs. (12)–(17) is indeed remarkable, in that it fits experimental results collected over a three-orders-of-magnitude change in the reactant partial pressures.

REFERENCES

1. Egelhoff, W. F., *in* "The Chemical Physics of Solid Surfaces and Heterogeneous Catalysis" (D. A. King and D. P. Woodruff, Eds.), Chap. 6. Elsevier, New York, 1982.
2. Harrison, B., Wyatt, M., and Gough, K. G., *Catalysis* **5,** Chap. 4 (1982).
3. Shelef, M., *Catal. Rev. Sci. Eng.* **11,** 1 (1975).
4. Taylor, K. C., and Schlatter, J. C., *J. Catal.* **63,** 53 (1980).
5. Taylor, K. C., *in* "The Catalytic Chemistry of Nitrogen Oxides" (R. L. Klimisch and J. G. Larson, Eds.), p. 173. Plenum, New York, 1975.
6. Kobylinski, T. P., and Taylor, B. W., *J. Catal.* **33,** 376 (1974).
7. Campbell, C. T., and White, J. M., *Appl. Surf. Sci.* **1,** 347 (1978).
8. Dubois, L. H., Hansma, P. K., and Somorjai, G. A., *J. Catal.* **65,** 318 (1980).
9. Rives-Arnau, V., and Munuera, G., *Appl. Surf. Sci.* **6,** 122 (1980).
10. Arai, H., and Tominaga, H., *J. Catal.* **43,** 131 (1976).
11. Unland, M., *J. Catal.* **31,** 459 (1973).
12. Solymosi, F., and Sarkany, J., *Appl. Surf. Sci.* **3,** 68 (1979).
13. Yao, H. C., Japar, S., and Shelef, M., *J. Catal.* **50,** 407 (1977).
14. Vavere, A., and Hansen, R. S., *J. Catal.* **69,** 158 (1981).
15. Mahaffy, P., and Hansen, R. S., *J. Chem. Phys.* **71**(4), 1853 (1979).
16. Castner, D. G., Sexton, B. A., and Somorjai, G. A., *Surf. Sci.* **71,** 519 (1978).
17. Baird, R. J., Ku, R. C., and Wynblatt, P., *Surf. Sci.* **97,** 346 (1980).
18. Castner, D. G., and Somorjai, G. A., *Surf. Sci.* **83,** 60 (1979).
19. Musket, R. G., McLean, W., Colmenares, C. A., Makowiecki, D. M., and Siekhaus, W. J., *Appl. Surf. Sci.* **10,** 143 (1982).
20. Dubois, L. H., and Somorjai, G. A., *Surf. Sci.* **91,** 514 (1980).
21. Semancik, S., Haller, G. L., and Yates, J. T., *Appl. Surf. Sci.* **10,** 546 (1982).
22. Bouwman, R., Van Mechelen, J. B., and Holscher, A. A., *J. Vac. Sci. Technol.* **15,** 91 (1978).
23. Dubois, L. H., *J. Chem. Phys.* **77**(10), 5228 (1982).
24. Yates, J. T., Williams, E. D., and Weinberg, W. H., *Surf. Sci.* **91,** 562 (1980).
25. Thiel, P. A., Yates, J. T., and Weinberg, W. H., *Surf. Sci.* **82,** 22 (1979).
26. Davis, L. E., MacDonald, N. C., Palmberg, G. E., Riach, G. E., and Weber, R. E., "Handbook of Auger Electron Spectroscopy," Physical Electronics Division of Perkin–Elmer Inc., Eden Prairie, Minn., 1976.
27. Redhead, P. A., *Vacuum* **12,** 203 (1962).
28. Campbell, C. T., and White, J. M., *J. Catal.* **54,** 289 (1978).
29. Ho, P., and White, J. M., *Surf. Sci.* **137,** 103 (1984).
30. Benziger, J. B., *Appl. Surf. Sci.* **6,** 105 (1980).
31. Broden, G., Rhodin, T. N., Brucker, C., Benbow, R., and Hurych, Z., *Surf. Sci.* **59,** 593 (1976).
32. Miyazaki, E., and Yasumori, I., *Surf. Sci.* **57,** 755 (1976).
33. Iizuka, T., and Lundsford, J., *J. Mol. Catal.* **8,** 391 (1980).
34. Hardee, J. R., and Hightower, J. W., *J. Catal.* **86,** 137 (1984).
35. Haskell, K. H., and Jones, R. E., "Brief Instructions for Using the Sandia Mathematical Subroutine Library," Chap. 8, Report No. SAND77-1441, Sandia National Laboratory, Albuquerque, N.Mex., 1978.
36. Ibach, H., and Lehwald, S., *Surf. Sci.* **76,** 1 (1978).
37. Gland, J. L., and Sexton, B. A., *Surf. Sci.* **94,** 355 (1980).